



**HAL**  
open science

## Optoelectronic Mixing in High-Mobility Graphene

L Hamidouche, A Montanaro, M Rosticher, E Grimaldi, B Poupet, T Taniguchi, K Watanabe, Bernard Plaçais, Emmanuel Baudin, P Legagneux

► **To cite this version:**

L Hamidouche, A Montanaro, M Rosticher, E Grimaldi, B Poupet, et al.. Optoelectronic Mixing in High-Mobility Graphene. ACS photonics, 2020, 8, pp.369 - 375. 10.1021/acsp Photonics.0c01679 . hal-03367950

**HAL Id: hal-03367950**

**<https://hal.science/hal-03367950>**

Submitted on 6 Oct 2021

**HAL** is a multi-disciplinary open access archive for the deposit and dissemination of scientific research documents, whether they are published or not. The documents may come from teaching and research institutions in France or abroad, or from public or private research centers.

L'archive ouverte pluridisciplinaire **HAL**, est destinée au dépôt et à la diffusion de documents scientifiques de niveau recherche, publiés ou non, émanant des établissements d'enseignement et de recherche français ou étrangers, des laboratoires publics ou privés.

## Optoelectronic Mixing in High-Mobility Graphene

L. Hamidouche,\* A. Montanaro, M. Rosticher, E. Grimaldi, B. Poupet, T. Taniguchi, K. Watanabe, B. Plaçais, E. Baudin, and P. Legagneux

Cite This: <https://dx.doi.org/10.1021/acsp Photonics.0c01679>

Read Online

ACCESS |



Metrics &amp; More



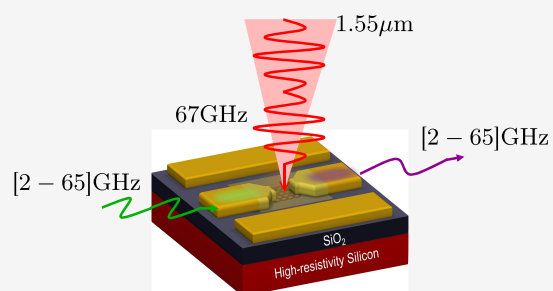
Article Recommendations



Supporting Information

**ABSTRACT:** High-mobility hexagonal boron nitride (hBN)/graphene/hBN heterostructures are able to reach intrinsic limits of transport. Here, we investigate optoelectronic mixing, which is a demanding function combining efficient photodetection and fast carrier dynamics. Using such a heterostructure embedded in a coplanar waveguide, we obtain a record conversion efficiency of about  $-40$  dB for frequencies up to 65 GHz. This performance is obtained at high doping in the photobolometric regime. We provide a microscopic model of the photodetection, which accurately describes the experimental observations, allows the assessment of the intrinsic limits of our device, and paves the way for device optimization by revealing the different mechanisms at play.

**KEYWORDS:** down-conversion efficiency, photoconductivity, photobolometric effect, electronic transport, cooling mechanism, scattering



An optoelectronic mixer is an electronic frequency converter controlled by an optical excitation. Optoelectronic mixing, which requires both efficient photodetection and high-speed transport, is one of the most demanding functions involving high-quality materials and advanced theoretical modeling. Graphene fulfills these requirements owing to its high carrier mobility, wide-range light absorption,<sup>1</sup> and low photocarrier lifetime.<sup>2</sup>

Graphene properties have already been exploited for high frequency electronics<sup>3–6</sup> and photodetection.<sup>2,7</sup> They have been exploited recently in a first high frequency (30 GHz) optoelectronic mixer.<sup>8</sup> The recent advances in graphene–boron nitride heterostructures provide nearly ballistic transport<sup>9,10</sup> where photodetection mechanisms approach the intrinsic limit. This raises the question of whether we can exploit the extraordinary properties of boron nitride-encapsulated graphene to push the performance of the optoelectronic mixers and reveal the underlying basic mechanisms.

Mixers are essential building blocks in modern communication and array antenna systems. Classically, electronic mixing operation consists in converting an incoming signal at a certain frequency to another frequency using a local oscillator. Both up- and down-conversion operations are possible. Mixers are very common in communication systems using electronic nonlinearities where signals are transmitted on a high carrier frequency over the communication media. At the receiver end, the signal is down-converted to near-zero frequency (baseband) to perform signal processing and extract the carried information. With optoelectronic mixing, the local oscillator (LO) is not an electrical signal but an optical one. This optical LO can easily be transmitted through optical fibers which, unlike RF cables, are lightweight and immune to electro-

magnetic interference. This is particularly advantageous in array antenna systems, which require the distribution of the LO signal to each individual antenna. The function of the optoelectronic mixer is thus to convert the LO signal from the optical to the electrical domain<sup>11–13</sup> and to mix this signal with the RF signal received by the antenna. Since graphene absorbs light at communication wavelengths (including  $1.55 \mu\text{m}$  wavelength used in optical fiber communications), it is an excellent choice for high frequency mixers.<sup>14</sup> Moreover, its compatibility with the already existing complementary metal oxide semiconductor (CMOS) technology<sup>2</sup> allows one to envision the manufacture of low-cost devices integrating the down-conversion function and signal processing.

In this Article, we use a hexagonal boron nitride (hBN)-encapsulated graphene in a coplanar waveguide (gCPW) structure to realize a high-speed, high-efficiency optoelectronic mixer at the telecom wavelength. Such high-quality graphene allows the demonstration of an optoelectronic mixer exhibiting a bandwidth larger than 65 GHz and a down-conversion efficiency of  $-40$  dB, i.e., 45 dB higher than the previous result.<sup>8</sup> This improvement stems from an increase of the absolute photoconductance, which boosts the photodetection efficiency. Microscopically, the increase in channel conductivity stems from the suppression of impurity scattering

Received: October 31, 2020

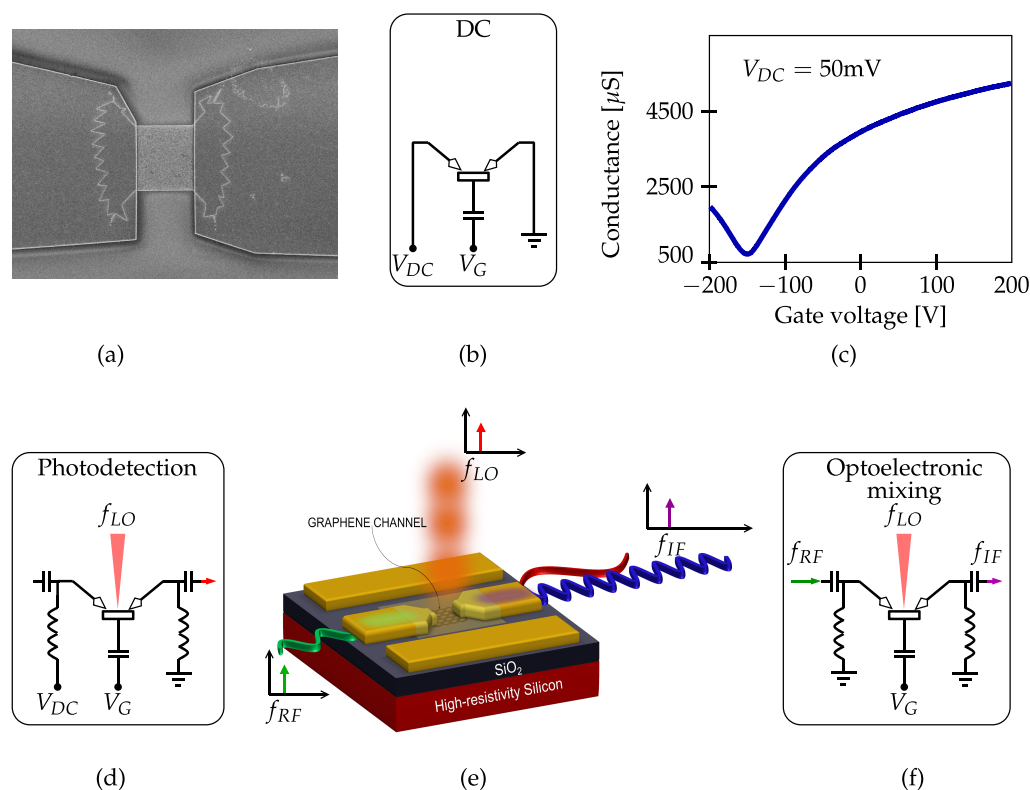


**Figure 1.** Fabricated device and experimental setups. (a) Scanning electron microscope image of the  $3 \mu\text{m} \times 3 \mu\text{m}$  hBN/G/hBN channel with Cr/Au (5 nm/100 nm) contacts, fabricated on a high resistivity silicon substrate covered by a  $2 \mu\text{m}$  thick thermal  $\text{SiO}_2$ . (b) DC experimental setup. (c) Gate voltage dependence of the device conductance. (d) Photodetection with a  $1.55 \mu\text{m}$  laser focused on the channel (spot diameter of  $2.5 \mu\text{m}$ ) and modulated at  $f_{LO}$ . (e) Schematic of the hBN/G/hBN channel embedded in the gap of the signal line of the gCPW. (f) This gCPW mixes an RF signal at  $f_{RF}$  with the photodetected signal at  $f_{LO}$  to deliver a signal at the intermediate frequency,  $f_{IF} = f_{LO} - f_{RF}$ .

(prominent in  $\text{SiO}_2$ -supported graphene), which is substituted by substrate-induced strain disorder in hBN-encapsulated graphene.<sup>15</sup> In this mechanism, the photodetection efficiency comes from the temperature dependence of screening,<sup>16</sup> which affects the scalar contribution of strain disorder to conductivity and ultimately governs the photobolometric response. This paper includes a thorough analysis of the underlying mechanisms affecting the graphene optoelectronic mixer performance, using both experimental results and a theoretical model.

## ■ DEVICE FABRICATION AND DC CHARACTERIZATION

The h-BN encapsulated graphene was fabricated according to ref 9 and subsequently transferred using a poly-propylene carbonate (PPC)-Scotch tape-PDMS stamps on a high-resistivity ( $10 \text{ k}\Omega\text{-cm}$ ) silicon substrate covered by  $2 \mu\text{m}$  thick thermal  $\text{SiO}_2$ . The top and bottom h-BN encapsulating crystals have a thickness of 25 and 40 nm, respectively. The stack is then etched to a butterfly shape using  $\text{CHF}_3/\text{O}_2$  plasma with a PMMA mask (defined by electron-beam lithography) to form the graphene channel. Finally, the Cr/Au (5 nm/100 nm) drain and source contacts were deposited to obtain a  $3 \mu\text{m} \times 3 \mu\text{m}$  h-BN/G/h-BN channel matching the optical beam waist (see Figure 1a).

Using the DC experimental setup of Figure 1b with  $V_{DC} = 50 \text{ mV}$ , we plot in Figure 1c the graphene conductance as a function of the voltage applied to the silicon substrate, acting as a back gate ( $V_G$ ). The charge neutrality point (CNP) gate voltage  $V_{CNP}$  is about  $-150 \text{ V}$ . Given the graphene channel

length ( $3 \mu\text{m}$ ), the electric field is low ( $\sim 0.016 \text{ V}/\mu\text{m}$ ) and the field-effect mobility is equal to  $44\,000 \text{ cm}^2/\text{V}\cdot\text{s}$ . This value is 20 times larger than the field-effect mobility obtained by Montanaro<sup>8</sup> in CVD-graphene on  $\text{SiO}_2/\text{Si}$ . We also estimated the contact resistance by fitting the total resistance with the following formula

$$R_{\text{tot}} = R_c + \frac{R_{g0}}{\sqrt{1 + \left(\frac{V_G - V_{CNP}}{\Delta V}\right)^2}}$$

where  $R_c$  is the contact resistance,  $V_G$  is the gate voltage,  $\Delta V = en^*/C_G$  is the characteristic voltage width of the resistivity curve and is related to the puddle electronic density  $n^* \sim 2.4 \times 10^{11} \text{ cm}^{-2}$ , and  $R_0$  is the channel intrinsic resistance ( $R_{g0} = \rho_0 L/W$ , where  $\rho_0$  is graphene resistivity at charge neutrality point and  $L$  and  $W$  are, respectively, the length and width of the channel, which are equal for our device). We deduce a contact resistance of  $130 \Omega$ , approaching the intrinsic limit ( $\sim 40 \Omega$  in our sample for a Fermi energy of  $0.1 \text{ eV}$ ).

As illustrated in Figure 1e, the h-BN/G/h-BN channel is embedded in the gap of the signal line of a gCPW with a characteristic impedance of  $50 \Omega$ . This structure allows one to perform high-frequency photodetection measurements according to the setup shown in Figure 1d, whereas Figure 1f describes the optoelectronic measurement experiment. The intensity-modulated laser beam with  $f_{LO}$  varying from 2 to 67 GHz is focused on the graphene channel with a spot size of  $2.5 \mu\text{m}$ .

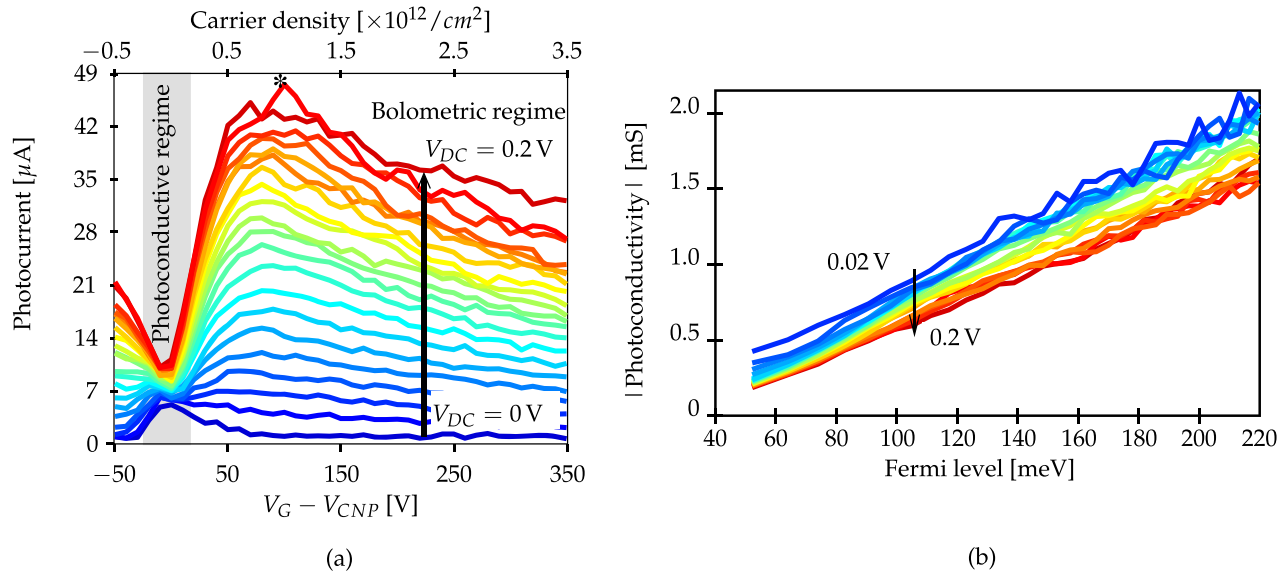


**Figure 2.** Photodetection measurements. (a) 67 GHz photocurrent amplitude as a function of  $V_G - V_{\text{CNP}}$  for  $V_{\text{DC}}$  biases varying from 0 to 0.2 V with a step of 0.01 V. Close to  $V_{\text{CNP}}$  (shaded region), the photocurrent and the optical signal are in phase. For  $|V_G - V_{\text{CNP}}| > 20$  V, they are opposite in phase. (b) Absolute value of the channel photoconductivity computed using eq 1 as a function of the Fermi level  $E_F$  [meV] =  $11.7\sqrt{V_G - V_{\text{CNP}}}$  (equivalent to the carrier density). Channel photoconductivity is negative and follows a linear variation.

## OPTOELECTRONIC PERFORMANCE

Figure 2a shows the amplitude of the 67 GHz photocurrent as a function of the gate voltage  $V_G - V_{\text{CNP}}$  for an increasing drain–source bias ( $V_{\text{DC}}$  varying from 0 to 0.2 V). Near CNP ( $|V_G - V_{\text{CNP}}| < 20$  V), the photocurrent results from the photoconductive effect, which is relatively small in this experiment but significant when the laser beam impinges on one of the graphene–metal contacts (see the Supporting Information). In this case, the photocurrent and the modulated optical signal are in-phase.<sup>8</sup>

For  $|V_G - V_{\text{CNP}}| > 20$  V, these signals are in opposite phase; i.e., the conductance decreases under illumination, indicating that the photocurrent results from a photobolometric effect.<sup>17</sup> This effect is a two-step process by which the incoming light heats the electron gas inducing a conductivity decrease. A photocurrent maximum is reached for  $V_G - V_{\text{CNP}} \sim 80$  V regardless of the bias value. Varying  $V_G - V_{\text{CNP}}$  from 50 to 300 V, the channel resistance decreases from 384 to 204  $\Omega$  whereas the contact resistance remains almost constant (130  $\Omega$ ). Thus, the channel bias decreases, and the photocurrent drops accordingly.

In order to shed light on the photocurrent mechanism, we plot in Figure 2b the channel photoconductivity as a function of the Fermi level according to the relation

$$\sigma_{\text{ph}}^{\text{RF}} = \frac{L}{W} \frac{I_{\text{ph}}}{V_{\text{DC}} - R_{\text{c}} I_{\text{DC}}} \left( 1 + \frac{(R_{\text{c}} + 2Z_0) I_{\text{DC}}}{V_{\text{DC}} - R_{\text{c}} I_{\text{DC}}} \right) \quad (1)$$

where the denominator accounts for the voltage drop within the graphene channel and the right-hand correction factor accounts for the RF impedance matching with the detection chain;  $Z_0 = 50 \Omega$  is the impedance of the measurement system (see the Supporting Information).

We observe in Figure 2b that, above 50 meV, the intrinsic photoconductivity is proportional to the Fermi energy, revealing that the observed saturation and decrease of the photocurrent in Figure 2a is due to the influence of the contact resistances as well as the impedance mismatch between the

device and the measurement system. The small decrease in photoconductivity with increasing bias is due to the current saturation effect in such a high-mobility device.<sup>10</sup>

We now turn to optoelectronic mixing. In this mode, as sketched in Figure 1e,f, the DC bias  $V_{\text{DC}}$  is substituted by a RF bias of power  $-20$  dBm and frequency  $f_{\text{RF}} = 2\text{--}65$  GHz, with the local oscillator frequency being fixed at  $f_{\text{LO}} = f_{\text{opt}} = 67$  GHz.

In the mixing mode, the applied voltage is a rapid and small variation around a zero DC bias. Therefore, the mixing current for a given Fermi level  $E_F$  can be written

$$I_{\text{mix}}(f_{\text{IF}}) = \frac{1}{2} G_{\text{ph}}^{\text{diff}}(f_{\text{opt}}) V_{\text{RF}}(f_{\text{RF}}) \quad (2)$$

where  $G_{\text{ph}}^{\text{diff}} = \frac{dI_{\text{ph}}}{dV_{\text{DC}}}$  is the differential photoconductance which, contrarily to  $\sigma_{\text{ph}}^{\text{RF}}$ , is experimentally measured with respect to  $V_{\text{DC}}$  and encompasses the two phenomena related to contact resistance and system impedance mismatch. It depends on  $E_F$  and is modulated at the laser modulation frequency  $f_{\text{opt}}$  and  $V_{\text{RF}}(f_{\text{RF}})$  is the applied RF voltage. The factor  $\frac{1}{2}$  comes from the fact that an up-converted current at  $f_{\text{opt}} + f_{\text{RF}}$  is also generated.

The voltage  $V_{\text{RF}}$  can be written in terms of the power  $P_{\text{RF}}$  delivered to the device taking into account the total impedance of the device  $Z_T$  and the measurement system impedance  $Z_0$  (50  $\Omega$  for our experimental setup) yielding

$$I_{\text{mix}}(f_{\text{IF}}) = G_{\text{ph}}^{\text{diff}}(f_{\text{opt}}) \frac{Z_T}{Z_T + 2Z_0} \sqrt{Z_0 P_{\text{RF}}} \quad (3)$$

The down-conversion efficiency can be written as

$$\frac{P_{\text{IF}}}{P_{\text{RF}}} = \frac{Z_0 I_{\text{mix}}^2}{P_{\text{RF}}} = \left( Z_0 G_{\text{ph}}^{\text{diff}} \frac{Z_T}{Z_T + 2Z_0} \right)^2 \quad (4)$$

When the reactive part of the device impedance is neglected,<sup>18</sup> it becomes

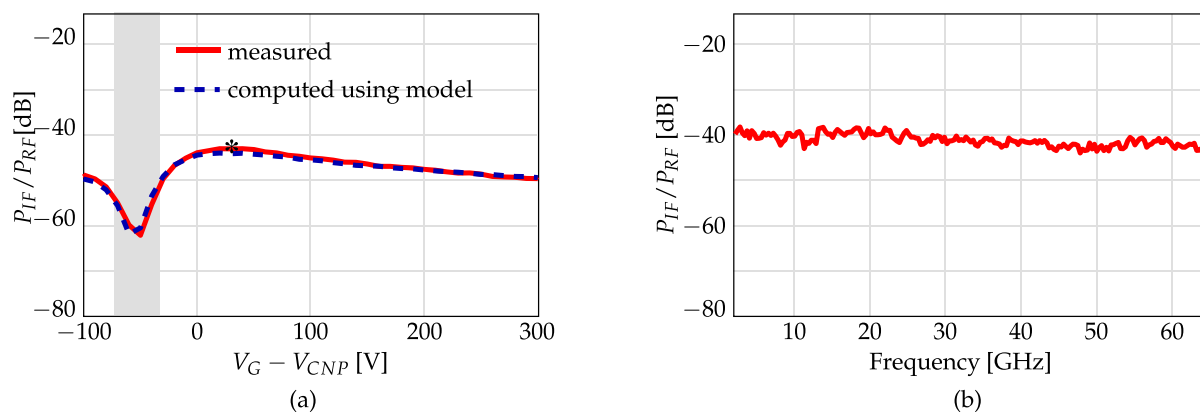


**Figure 3.** Optoelectronic mixing measurements for  $f_{\text{opt}} = 67$  GHz. (a) Comparison of the power conversion efficiency calculated from the photoresponse (blue dashed curve) at 67 GHz with the amplitude of the measured power conversion efficiency at  $f_{\text{IF}} = 65$  GHz (red curve) with respect to gate voltage  $V_G - V_{\text{CNP}}$ . (b) Power conversion efficiency ( $P_{\text{IF}}/P_{\text{RF}}$ ) as a function of the intermediate frequency  $f_{\text{IF}}$  for  $V_G - V_{\text{CNP}} = 80$  V.

$$\frac{P_{\text{IF}}}{P_{\text{RF}}} = \left( R_0 G_{\text{ph}}^{\text{diff}} \frac{R_T}{R_T + 2R_0} \right)^2 \quad (5)$$

For a large  $W/L$  value and low contact resistance, eq 5 reduces to  $\left( \frac{1}{2} G_{\text{ph}}^{\text{diff}} \times R_g \right)^2$  where  $R_g$  is the channel resistance.

Figure 3a shows the power down-conversion efficiency (blue dashed curve) computed with eq 5 using the derivative of the measured photocurrent measured at various gate voltages. It is compared to the actually measured power conversion efficiency (red curve). The very good agreement between the computed and experimental values validates this simple model.

Figure 3b shows that the conversion efficiency  $P_{\text{IF}}/P_{\text{RF}}$  is constant with frequency, indicating that our gCPW device has a bandwidth larger than 65 GHz. In the doped regime considered here, the heat conductance of the device is limited by the contact thermal resistance, which according to the Wiedeman-Franz law, is upper bounded by  $R_{\text{th}} < \frac{R_c/4}{\mathcal{L}T_{\text{ph}}}$ . From

this, we deduce an upper bound for the characteristic thermalization time of the hBN-encapsulated optoelectronic mixer of  $\tau_{\text{th}} \approx R_{\text{th}} C_{\text{th}} \approx 7.5$  ps, where the characteristic heat capacity of hBN-encapsulated monolayer graphene is  $C = c_p LW$ , with  $c_p \approx 1.8 \times 10^{-7} \text{ J}\cdot\text{K}^{-1}\cdot\text{m}^{-2}$ .<sup>19</sup> This explains the ultrafast response of the device enabling microwave optoelectronic mixing.

The obtained conversion efficiency of  $-40$  dB is more than 4 orders of magnitude higher than the previously obtained value of  $-85$  dB by Montanaro et al.<sup>8</sup> This means that the carrier mobility of the graphene layer integrated in the gCPW is a crucial parameter to the optoelectronic mixing performance, which raises the question of an upper performance limit.

## DISCUSSION

We now turn our attention to the photodetection mechanism. The absorbed photon energy from the incoming near-infrared light is mostly transferred to the electron gas with two important consequences: (i) the buildup of an electron–hole distribution and (ii) a hot carrier multiplication effect because each photon energy  $h\nu$  promotes the characteristic energy  $k_B T_e$  of many electrons via Auger scattering. At large doping, the temperature increase upon illumination leads to an increase of the channel resistance, resulting in a negative photoconductance (NPC).

The physical origin of NPC depends on frequency. At low frequency, both electron and phonon temperatures increase with optical power, leading to an increase of the phonon resistivity, at least in high-mobility graphene as recently investigated in ref 20. The situation is different at high frequency where lattice temperature is decoupled, and the modulation of the electronic temperature is the main source of photoresistance. The origin lies in the reduction in screening of both impurity and lattice disorder potentials with electronic temperature.<sup>16</sup> The frequency crossover, in the tens of MHz range,<sup>20</sup> involves the electron–phonon thermal coupling and the phonon heat capacity.

The photobolometric effect has first been observed in low-mobility graphene (graphene on  $\text{SiO}_2$ ),<sup>17</sup> where it is revealed by a NPC at large doping. However, at low doping, this manifestation is obscured by the dominant positive photoconductance (PPC) due to the ambipolar conduction produced by electron–hole pair generation.<sup>21</sup> In contrast, with the high-mobility device considered in this study, PPC is limited to a very small doping range ( $|n| \lesssim 0.2 \times 10^{12} \text{ cm}^{-2}$ ). The low doping threshold for the disappearance of PPC is specific to high-mobility graphene in which electron scattering is dominated by electron–electron collisions, and the current from the majority carriers drags the minority carriers due to electron–hole viscous drag.<sup>22,23</sup> As a consequence, the total current is proportional to the total charge density but is mostly unaffected by the number of electron–hole pairs induced by illumination and involved in transport.<sup>22</sup>

To quantitatively compare the photobolometric effect in low- and high-mobility graphene, it is necessary to first consider electronic temperatures reached under illumination in each case. The electronic temperature results from the competition between the electron gas heating by light absorption and its cooling by contact with its environment. For graphene on  $\text{SiO}_2$ , energy transfer is dominated by supercollision cooling due to short-range scatterers.<sup>24–26</sup> In contrast, in high-mobility hBN-encapsulated graphene, supercollision cooling is suppressed and the dominant cooling mechanisms are electronic heat conduction to the leads (in-plane heat transfer) and hyperbolic phonon polariton radiative cooling (out-of-plane heat transfer; see the Supporting Information). At low doping, electronic heat conduction is limited by the channel thermal conductance, but at large doping, it is limited by thermal contact resistance. In parallel to

in-plane heat transfer, the hot electron gas radiates energy in the hyperbolic phonon polariton branches of hBN (dressed OP phonons).<sup>19,27</sup> The out-of-plane radiative cooling efficiency is independent of the electronic mobility, whereas, according to the Wiedeman-Franz law, the in-plane electronic heat conduction is proportional to the electronic mobility.

To shed light on the photobolometric mechanism at play in hBN-encapsulated graphene, Table 1 compares the photo-

**Table 1. Comparison of Photothermoelectric Effect between Low- and High-Mobility Graphene<sup>a</sup>**

	device (a): ref 17	device (b): see the Supporting Information	device (c): this work
$L \times w$ [ $\mu\text{m} \times \mu\text{m}$ ]	$6 \times 1$	$10 \times 6$	$3 \times 3$
$\mu$ [ $\text{cm}^2 \cdot \text{V}^{-1} \cdot \text{s}^{-1}$ ]	$\sim 2700$	4800	$\sim 44\,000$
$\sigma$ [mS]	0.6	1.1	10
method	optical, 1.1 kHz	optical, 0.7 kHz	optical, 67 GHz
$\sigma_{\text{ph}}$ [ $\mu\text{S}$ ]	-0.7	-45	-800
$P_{\text{inc}}$ [mW]	0.37	30	100
$\lambda$ [ $\mu\text{m}$ ]	0.69	1.55	1.55
dominant cooling mechanism	supercollisions	supercollisions	electronic heat conduction/ HPhP radiation
$\overline{\Delta T_e}$ [K]	3.7	41	940
conduction mechanism	Coulombian impurity- limited	Coulombian impurity- limited	random strain- limited
$\chi_{\text{exp}} = \frac{\sigma_{\text{ph}} E_{\text{F}}}{\sigma k_{\text{B}} \overline{\Delta T_e}}$	-0.43	-1.27	-0.12
Bolometric theory	-1	-1	-[0.01; 0.080]

<sup>a</sup>The temperature rise  $\overline{\Delta T_e}$  is computed using the methods described in the Supporting Information.

bolometric effect for three devices with different mobilities: (a) the graphene on SiO<sub>2</sub> device considered in ref 17, (b) a graphene on SiO<sub>2</sub> capped with Al<sub>2</sub>O<sub>3</sub> used as a reference for this study, and (c) the hBN-encapsulated graphene device.

The temperature increase is deduced from the power balance between the absorbed incident laser power and (i) supercollision cooling for the two graphene-on-SiO<sub>2</sub> devices (a) and (b) (see the Supporting Information) or (ii) electronic heat conduction for hBN-encapsulated graphene (see the Supporting Information). Device (b) is interesting because it bridges the gap between the experiments of (a) and (c): Device (b) has similar characteristics as (a) but is excited at the same wavelength and characteristic laser power as (c). To compare the experiments (a), (b), and (c), we assume that the dependence on the irradiation wavelength is irrelevant as most of the photon energy goes in the electronic bath.

The electronic temperature increase results in a reduced screening of the scattering centers of the electrostatic potentials (Coulombian impurities, ripples). As a consequence, electronic conductivity decreases when the light is shone on the graphene channel. This observed negative photoconductance is the experimental signature of the photobolometric effect. For room temperature devices, the thermoconductance change is  $\Delta\sigma \simeq \chi\sigma \frac{k_{\text{B}}\overline{\Delta T_e}}{E_{\text{F}}}$ , where  $\chi$  is the thermobolometric coefficient, which should approach -1.0 according to theory (see the Supporting Information).

Table 1 reports the values of the experimentally deduced thermobolometric coefficient  $\chi_{\text{exp}}$  for the low-mobility graphene (devices (a) and (b)) and the high-mobility graphene (device (c)). Whereas both graphene-on-SiO<sub>2</sub> devices (a) and (b) present values in line with the theoretical expectations, the hBN-encapsulated graphene device's coefficient is strikingly smaller. This observation is emblematic of high-mobility graphene: hBN encapsulation leads to a high carrier mobility ( $\mu > 40\,000 \text{ cm}^2/\text{V}\cdot\text{s}$ ), and Coulomb impurities are inherently absent. For this kind of high-mobility devices, several studies<sup>15,28</sup> have shown that mobility is limited by strain disorder. Strain disorder brings two contributions to the electron dynamics. The first is due to the random scalar potential (s), and the second is due to the random gauge potential (g). The random scalar potential leads to a mobility  $\mu_{\text{s}}$  which has the same sensitivity to electronic screening as the Coulomb impurity carrier mobility  $\mu_{\text{c}}$ . In contrast, the dominant gauge potential contribution is independent of screening. Therefore, under illumination, the relative variation of the photoconductivity  $\frac{\Delta\sigma}{\sigma} = \frac{\Delta\mu}{\mu}$  is the same for Coulomb impurity scattering and for the random scalar potential. In high-mobility devices, the electronic mobility consists of the scalar and gauge potential contributions:  $\mu^{-1} = \mu_{\text{s}}^{-1} + \mu_{\text{g}}^{-1}$  and

$$\frac{\Delta\mu}{\mu} \Big|_{\text{hBN}} = \left( \frac{\mu_{\text{s}}}{\mu_{\text{g}}} \right) \frac{\Delta\mu}{\mu} \Big|_{\text{SiO}_2}$$

large uncertainty in the theoretical estimate is mainly due to the square dependence in the deformation potential values, which are not well-known parameters.) for  $\mu_{\text{s}}$  and  $\mu_{\text{g}}$  allows one to compute a reduction in the relative conductivity by a factor of  $\frac{\mu_{\text{s}}}{\mu_{\text{g}}} \simeq [0.01; 0.08]$ , depending on the exact value of the

electron-phonon coupling strength (see the Supporting Information). The experimental thermobolometric coefficient  $\chi_{\text{exp}} \simeq 0.12$  deduced from Table 1 approaches this calculated range but remains slightly larger, presumably due to the few remaining Coulombian impurities within the sample.

Therefore, when one compares devices with increasing carrier mobility, this coefficient tends to decrease because the carrier mobility turns from Coulombian impurity scattering limited to random gauge potential scattering. However, the photoconductivity, which quantifies the intrinsic efficiency of the complete photothermoelectric process, is the product of the thermobolometric coefficient  $\chi$  by the laser-induced temperature increase  $\Delta T$  and the graphene conductance  $\sigma$  at fixed laser power and doping. Consequently, with increasing carrier mobility, photoconductance first increases rapidly with carrier mobility as conductance increases and supercollision cooling is suppressed, yielding a larger channel temperature, and then slows down due to the reduced thermobolometric coefficient.

To summarize, our comparison reveals that high-mobility hBN-encapsulated graphene transistors are dissimilar in two ways with respect to lower mobility graphene devices: (i) the cooling mechanisms of the electron gas are radically different, and (ii) the conduction mechanisms at stake are also less sensitive to electronic screening and, therefore, to a temperature rise.

## CONCLUSION

We have reported an in-depth study of a 65 GHz optoelectronic mixer made of an hBN/graphene/hBN

heterostructure embedded in a coplanar waveguide. We have observed a record mixing conversion efficiency of around  $-40$  dB over the whole bandwidth, 45 dB higher than previously reported, and quantitatively related this figure to the device transport and photodetection performances.

We proposed a microscopic model of the photobolometric detection in high-mobility graphene, supported by experimental observations on three devices, which explains the photodetection performance with respect to low-mobility graphene, resulting from the competition between two phenomena: the suppression of the supercooling mechanism and the change in electronic scattering mechanism sensitivity to electronic screening. They both enhance the photodetection efficiency by increasing the photothermal effect and electronic outcoupling, respectively.

The quantitative understanding of optoelectronic mixing in graphene and its intrinsic limits brought by this work opens the door to rational device optimization. Beyond this exploratory work, in which the graphene channel was illuminated by a free space laser beam, an important performance boost will also be gained by increasing light absorption via an integrated photonic circuit.

## ■ ASSOCIATED CONTENT

### SI Supporting Information

The Supporting Information is available free of charge at <https://pubs.acs.org/doi/10.1021/acsphotonics.0c01679>.

Photodetection; intrinsic photoconductivity; cooling mechanisms (PDF)

## ■ AUTHOR INFORMATION

### Corresponding Author

L. Hamidouche – *Thales Research & Technology, 91767 Palaiseau, France*; [orcid.org/0000-0002-6253-5145](https://orcid.org/0000-0002-6253-5145);  
Email: [louiza.hamidouche@thalesgroup.com](mailto:louiza.hamidouche@thalesgroup.com)

### Authors

A. Montanaro – *Thales Research & Technology, 91767 Palaiseau, France*

M. Rosticher – *Laboratoire de Physique de l'École Normale Supérieure, ENS, Université PSL, CNRS, Sorbonne Université, Université Sorbonne Paris Cité, 75005 Paris, France*

E. Grimaldi – *Thales Research & Technology, 91767 Palaiseau, France*

B. Poupet – *Thales Research & Technology, 91767 Palaiseau, France*

T. Taniguchi – *Advanced Materials Laboratory, National Institute of Materials Science, Tsukuba, Ibaraki 305-0047, Japan*; [orcid.org/0000-0002-1467-3105](https://orcid.org/0000-0002-1467-3105)

K. Watanabe – *Advanced Materials Laboratory, National Institute of Materials Science, Tsukuba, Ibaraki 305-0047, Japan*; [orcid.org/0000-0003-3701-8119](https://orcid.org/0000-0003-3701-8119)

B. Plaçais – *Laboratoire de Physique de l'École Normale Supérieure, ENS, Université PSL, CNRS, Sorbonne Université, Université Sorbonne Paris Cité, 75005 Paris, France*

E. Baudin – *Laboratoire de Physique de l'École Normale Supérieure, ENS, Université PSL, CNRS, Sorbonne Université, Université Sorbonne Paris Cité, 75005 Paris, France*

P. Legagneux – *Thales Research & Technology, 91767 Palaiseau, France*

Complete contact information is available at:  
<https://pubs.acs.org/10.1021/acsphotonics.0c01679>

### Notes

The authors declare no competing financial interest.

## ■ ACKNOWLEDGMENTS

We acknowledge that this project has received funding from the European Union's Horizon program under grant agreement no. 785219 (Core2) and no. 881603 (Core3) Graphene Flagship.

## ■ REFERENCES

- (1) Mak, K. F.; Sfeir, M. Y.; Wu, Y.; Lui, C. H.; Misewich, J. A.; Heinz, T. F. Measurement of the Optical Conductivity of Graphene. *Phys. Rev. Lett.* **2008**, *101*, 196405.
- (2) Ferrari, A. C.; Bonaccorso, F.; Fal'ko, V.; Novoselov, K. S.; Roche, S.; Bøggild, P.; Borini, S.; Koppens, F. H. L.; Palermo, V.; Pugno, N.; Garrido, J. A.; Sordan, R.; Bianco, A.; Ballerini, L.; Prato, M.; Lidorikis, E.; Kivioja, J.; Marinelli, C.; Ryhänen, T.; Morpurgo, A.; Coleman, J. N.; Nicolosi, V.; Colombo, L.; Fert, A.; Garcia-Hernandez, M.; Bachtold, A.; Schneider, G. F.; Guinea, F.; Dekker, C.; Barbone, M.; Sun, Z.; Galiotis, C.; Grigorenko, A. N.; Konstantatos, G.; Kis, A.; Katsnelson, M.; Vandersypen, L.; Loiseau, A.; Morandi, V.; Neumaier, D.; Treossi, E.; Pellegrini, V.; Polini, M.; Tredicucci, A.; Williams, G. M.; Hee Hong, B.; Ahn, J.-H.; Min Kim, J.; Zirath, H.; van Wees, B. J.; van der Zant, H.; Occhipinti, L.; Di Matteo, A.; Kinloch, I. A.; Seyller, T.; Quesnel, E.; Feng, X.; Teo, K.; Rupasinghe, N.; Hakonen, P.; Neil, S. R. T.; Tannock, Q.; Löfwander, T.; Kinaret, J. Science and technology roadmap for graphene, related two-dimensional crystals, and hybrid systems. *Nanoscale* **2015**, *7* (11), 4598–4810.
- (3) Lin, Y.-M.; Dimitrakopoulos, C.; Jenkins, K. A.; Farmer, D. B.; Chiu, H.-Y.; Grill, A.; Avouris, P. 100-GHz Transistors from Wafer-Scale Epitaxial Graphene. *Science* **2010**, *327*, 662.
- (4) Pallecchi, E.; Benz, C.; Betz, A. C.; Löhneysen, H. v.; Plaçais, B.; Danneau, R. Graphene microwave transistors on sapphire substrates. *Appl. Phys. Lett.* **2011**, *99*, 113502.
- (5) Wei, W.; Pallecchi, E.; Haque, S.; Borini, S.; Avramovic, V.; Centeno, A.; Amaia, Z.; Happy, H. Mechanically robust 39 GHz cut-off frequency graphene field effect transistors on flexible substrates. *Nanoscale* **2016**, *8* (29), 14097–14103.
- (6) Vitiello, M.; Cadore, A. R.; Yang, X.; Vorobiev, A.; Muench, J. E.; Watanabe, K.; Taniguchi, T.; Stake, J.; Ferrari, A. C.; Vitiello, M. S. Thermoelectric graphene photodetectors with sub-nanosecond response times at terahertz frequencies. *Nanophotonics* **2020**, *10*, 89.
- (7) Koppens, F. H. L.; Mueller, T.; Avouris, P.; Ferrari, A. C.; Vitiello, M. S.; Polini, M. Photodetectors based on graphene, other two-dimensional materials and hybrid systems. *Nat. Nanotechnol.* **2014**, *9*, 780–793.
- (8) Montanaro, A.; Mzali, S.; Mazellier, J.-P.; Bezencenet, O.; Larat, C.; Molin, S.; Morvan, L.; Legagneux, P.; Dolfi, D.; Dlubak, B.; Seneor, P.; Martin, M.-B.; Hofmann, S.; Robertson, J.; Centeno, A.; Zurutuza, A. Thirty Gigahertz Optoelectronic Mixing in Chemical Vapor Deposited Graphene. *Nano Lett.* **2016**, *16*, 2988–2993.
- (9) Banzerus, L.; Schmitz, M.; Engels, S.; Dauber, J.; Oellers, M.; Haupt, F.; Watanabe, K.; Taniguchi, T.; Beschoten, B.; Stampfer, C. Ultrahigh-mobility graphene devices from chemical vapor deposition on reusable copper. *Science Advances* **2015**, *1*, No. e1500222.
- (10) Wilmart, Q.; Boukhicha, M.; Graef, H.; Mele, D.; Palomo, J.; Rosticher, M.; Taniguchi, T.; Watanabe, K.; Bouchiat, V.; Baudin, E.; Berroir, J.-M.; Bocquillon, E.; Fève, G.; Pallecchi, E.; Plaçais, B. High-Frequency Limits of Graphene Field-Effect Transistors with Velocity Saturation. *Appl. Sci.* **2020**, *10*, 446.

(11) Morvan, L.; Lai, N. D.; Dolfi, D.; Huignard, J.-P.; Brunel, M.; Bretenaker, F.; Le Floch, A. Building blocks for a two-frequency laser lidar-radar: a preliminary study. *Appl. Opt.* **2002**, *41*, 5702.

(12) Ruff, W. C.; Bruno, J. D.; Kennerly, S. W.; Ritter, K.; Shen, P. H.; Stann, B. L.; Stead, M. R.; Sztankay, Z. G.; Tobin, M. S. Self-mixing detector candidates for an FM/cw lidar architecture. *Proc. SPIE 4035, Laser Radar Technology and Applications V*, Sept 5, 2000, Orlando, FL; p 152.

(13) Chizh, A.; Malyshev, S. Fiber-optic system for local-oscillator signal distribution in active phased arrays. *2014 11th European Radar Conference*, Oct 2014, Rome, Italy; IEEE, 2014; pp 439–442.

(14) Nair, R. R.; Blake, P.; Grigorenko, A. N.; Novoselov, K. S.; Booth, T. J.; Stauber, T.; Peres, N. M. R.; Geim, A. K. Fine Structure Constant Defines Visual Transparency of Graphene. *Science* **2008**, *320*, 1308.

(15) Couto, N. J.; Costanzo, D.; Engels, S.; Ki, D.-K.; Watanabe, K.; Taniguchi, T.; Stampfer, C.; Guinea, F.; Morpurgo, A. F. Random Strain Fluctuations as Dominant Disorder Source for High-Quality On-Substrate Graphene Devices. *Phys. Rev. X* **2014**, *4*, 041019.

(16) Tomadin, A.; Hornett, S. M.; Wang, H. I.; Alexeev, E. M.; Candini, A.; Coletti, C.; Turchinovich, D.; Kläui, M.; Bonn, M.; Koppens, F. H. L.; Hendry, E.; Polini, M.; Tielrooij, K.-J. The ultrafast dynamics and conductivity of photoexcited graphene at different Fermi energies. *Science Advances* **2018**, *4*, No. eaar5313.

(17) Freitag, M.; Low, T.; Xia, F.; Avouris, P. Photoconductivity of biased graphene. *Nat. Photonics* **2013**, *7*, 53.

(18) Graef, H.; Mele, D.; Rosticher, M.; Banszerus, L.; Stampfer, C.; Taniguchi, T.; Watanabe, K.; Bocquillon, E.; Fève, G.; Berroir, J.-M.; Teo, E. H. T.; Plaçais, B. Ultra-long wavelength Dirac plasmons in graphene capacitors. *Journal of Physics: Materials* **2018**, *1*, 01LT02.

(19) Tielrooij, K.-J.; Hesp, N. C. H.; Principi, A.; Lundeberg, M. B.; Pogna, E. A. A.; Banszerus, L.; Mics, Z.; Massicotte, M.; Schmidt, P.; Davydovskaya, D.; Purdie, D. G.; Goykhman, I.; Soavi, G.; Lombardo, A.; Watanabe, K.; Taniguchi, T.; Bonn, M.; Turchinovich, D.; Stampfer, C.; Ferrari, A. C.; Cerullo, G.; Polini, M.; Koppens, F. H. L. Out-of-plane heat transfer in van der waals stacks through electron-hyperbolic phonon coupling. *Nat. Nanotechnol.* **2018**, *13*, 41–46.

(20) Yuan, S.; Yu, R.; Ma, C.; Deng, B.; Guo, Q.; Chen, X.; Li, C.; Chen, C.; Watanabe, K.; Taniguchi, T.; García de Abajo, F. J.; Xia, F. Room Temperature Graphene Mid-Infrared Bolometer with a Broad Operational Wavelength Range. *ACS Photonics* **2020**, *7*, 1206–1215.

(21) Frenzel, A.; Lui, C.; Shin, Y.; Kong, J.; Gedik, N. Semiconducting-to-Metallic Photoconductivity Crossover and Temperature-Dependent Drude Weight in Graphene. *Phys. Rev. Lett.* **2014**, *113*, 056602.

(22) Nam, Y.; Ki, D.-K.; Soler-Delgado, D.; Morpurgo, A. F. Electron hole collision limited transport in charge neutral bilayer graphene. *Nat. Phys.* **2017**, *13*, 1207–1214.

(23) Svintsov, D.; Vyurkov, V.; Yurchenko, S.; Otsuji, T.; Ryzhii, V. Hydrodynamic model for electron-hole plasma in graphene. *J. Appl. Phys.* **2012**, *111*, 083715.

(24) Betz, A. C.; Jhang, S. H.; Pallecchi, E.; Ferreira, R.; Fève, G.; Berroir, J.-M.; Plaçais, B. Supercollision cooling in undoped graphene. *Nat. Phys.* **2013**, *9*, 109–112.

(25) Graham, M. W.; Shi, S.-F.; Ralph, D. C.; Park, J.; McEuen, P. L. Photocurrent measurements of supercollision cooling in graphene. *Nat. Phys.* **2013**, *9*, 103–108.

(26) Ma, Q.; Gabor, N. M.; Andersen, T. I.; Nair, N. L.; Watanabe, K.; Taniguchi, T.; Jarillo-Herrero, P. Competing Channels for Hot-Electron Cooling in Graphene. *Phys. Rev. Lett.* **2014**, *112*, 247401.

(27) Yang, W.; Berthou, S.; Lu, X.; Wilmart, Q.; Denis, A.; Rosticher, M.; Taniguchi, T.; Watanabe, K.; Fève, G.; Berroir, J.-M.; Zhang, G.; Voisin, C.; Baudin, E.; Plaçais, B. A graphene zener-klein transistor cooled by a hyperbolic substrate. *Nat. Nanotechnol.* **2018**, *13*, 47–52.

(28) Wang, L.; Makk, P.; Zihlmann, S.; Baumgartner, A.; Indolese, D. I.; Watanabe, K.; Taniguchi, T.; Schönenberger, C. Mobility Enhancement in Graphene by *in situ* Reduction of Random Strain Fluctuations. *Phys. Rev. Lett.* **2020**, *124*, 157701.